

Influences of divalent ion substitution on the magnetic and dielectric properties of W-type barium ferrite

Shiyue He(何诗悦), Ruoshui Liu(刘若水), Xujie Liu(刘煦婕), Xianping Ye(叶先平), Lichen Wang(王利晨), and Baogen Shen(沈保根)

Citation: Chin. Phys. B, 2024, 33 (**6**): 066801. DOI: 10.1088/1674-1056/ad39d5
Journal homepage: http://cpb.iphy.ac.cn; http://iopscience.iop.org/cpb

What follows is a list of articles you may be interested in

Polarization Raman spectra of graphene nanoribbons

Wangwei Xu(许望伟), Shijie Sun(孙诗杰), Muzi Yang(杨慕紫), Zhenliang Hao(郝振亮), Lei Gao(高蕾), Jianchen Lu(卢建臣), Jiasen Zhu(朱嘉森), Jian Chen(陈建), and Jinming Cai(蔡金明)
Chin. Phys. B, 2023, 32 (**4**): 046803. DOI: 10.1088/1674-1056/ac80b3

In-plane optical anisotropy of two-dimensional VOCl single crystal with weak interlayer interaction

Ruijie Wang(王瑞洁), Qilong Cui(崔其龙), Wen Zhu(朱文), Yijie Niu(牛艺杰), Zhanfeng Liu(刘站锋), Lei Zhang(张雷), Xiaojun Wu(武晓君), Shuangming Chen(陈双明), and Li Song(宋礼)
Chin. Phys. B, 2022, 31 (**9**): 096802. DOI: 10.1088/1674-1056/ac7555

Ohmic and Schottky contacts of hydrogenated and oxygenated boron-doped single-crystal diamond with hill-like polycrystalline grains

Jing-Cheng Wang(王旌丞), Hao Chen(陈浩), Lin-Feng Wan(万琳丰), Cao-Yuan Mu(牟草源), Yao-Feng Liu(刘尧峰), Shao-Heng Cheng(成绍恒), Qi-Liang Wang(王启亮), Liu-An Li(李柳暗), and Hong-Dong Li(李红东)
Chin. Phys. B, 2021, 30 (**9**): 096803. DOI: 10.1088/1674-1056/ac032b

Formation of high-Sn content polycrystalline GeSn films by pulsed laser annealing on co-sputtered amorphous GeSn on Ge substrate

Lu Zhang(张璐), Hai-Yang Hong(洪海洋), Yi-Sen Wang(王一森), Cheng Li(李成), Guang-Yang Lin(林光杨), Song-Yan Chen(陈松岩), Wei Huang(黄巍), Jian-Yuan Wang(汪建元)
Chin. Phys. B, 2017, 26 (**11**): 116802. DOI: 10.1088/1674-1056/26/11/116802

Effect of substrate temperature on the morphological, structural, and optical properties of RF sputtered $Ge_{1-x}Sn_x$ films on Si substrate

H Mahmodi, M R Hashim
Chin. Phys. B, 2017, 26 (**5**): 056801. DOI: 10.1088/1674-1056/26/5/056801

Influences of divalent ion substitution on the magnetic and dielectric properties of W-type barium ferrite

Shiyue He(何诗悦)[1,2,3], Ruoshui Liu(刘若水)[3], Xujie Liu(刘煦婕)[3], Xianping Ye(叶先平)[3], Lichen Wang(王利晨)[3,†], and Baogen Shen(沈保根)[1,2,3,4,‡]

[1] *School of Rare Earths, University of Science and Technology of China, Hefei* 230026, *China*
[2] *Ganjiang Innovation Academy, Chinese Academy of Sciences, Ganzhou* 341119, *China*
[3] *Ningbo Institute of Materials Technology & Engineering, Chinese Academy of Sciences, Ningbo* 315201, *China*
[4] *Beijing National Laboratory for Condensed Matter Physics, Institute of Physics, Chinese Academy of Sciences, Beijing* 100190, *China*

(Received 17 February 2024; revised manuscript received 3 April 2024; accepted manuscript online 3 April 2024)

Saturation magnetization, magneto-crystalline anisotropy field, and dielectric properties are closely related to microwave devices applied at different frequencies. For regulating the magnetic and dielectric properties of W-type barium ferrites, single-phase $BaMe_2Fe_{16}O_{27}$ (Me = Fe, Mn, Zn, Ni, Co) with different Me ions were synthesized by the high-temperature solid-state method. The saturation magnetization (M_s) range from 47.77 emu/g to 95.34 emu/g and the magnetic anisotropy field (H_a) range from 10700.60 Oe (1 Oe = 79.5775 A·m^{-1}) to 13739.57 Oe, depending on the type of cation substitution in the hexagonal lattice. The dielectric permittivity and dielectric loss decrease with increasing frequency of the AC electric field in the low-frequency region, while they almost remain constant in the high-frequency region. The characteristics of easy regulation and preparation make it a potential candidate for use in microwave device applications.

Keywords: W-type hexaferrite, Raman spectra, magnetic properties, dielectric properties

PACS: 68.55.Ln, 75.30.Gw, 75.47.Lx, 87.64.kp **DOI:** 10.1088/1674-1056/ad39d5

1. Introduction

Hexagonal ferrites, discovered in the 1950s,[1] have been classified into M, W, X, Y, Z, and U types based on the crystal structure.[2] These kinds of materials were found with excellent properties of low electrical conductivity, large saturation magnetization, and outstanding chemical stability, making them an ideal material for applications such as permanent magnets, high-density vertical magnetic recording media, microwave devices and absorption, stealth technology, and multiferroic materials.[3–7] Furthermore, their unique structure and magnetic anisotropy outperform other materials in self-bias high-frequency applications.[8] M-type ferrite has been widely studied due to its simple crystal structure and easy phase formation characteristics. It has become the most well-known and commercially used hard magnet ferrite and is used in microwave devices.[9] However, the regulation of the magnetic performance of M-type ferrite has nearly reached its limitation and makes further rapid improvement very challenging. In contrast, W-type ferrite has almost the same saturation magnetization M_s, more lattice sites than M-type and widely tunable magnetic properties, demonstrating the advantages of W-type hexagonal ferrite in microwave applications.[10–12]

The chemical formula of W-type ferrite is $AMe_2Fe_{16}O_{27}$ (where A = Sr or Ba, Me = Fe, Mg, Mn, Co, Ni, Cu, Zn). Its crystal structure is similar to that of M-type ferrite. It is composed of spinel blocks (S-blocks) and hexagonal blocks (R-blocks), stacking along the c axis and with the order of RSSR*S*S*. Here * indicates a 180° rotation of the block around the c axis. Figure 1 shows the schematic diagram of the W-type barium ferrite unit cell. The cations occupy seven different lattice sites, including four octahedral sites (12k, 4f_{VI}, 4f, and 6g), two tetrahedral sites (4e and 4f_{IV}), and one trigonal bipyramidal site (2d). Magnetic moments on the 12k, 6g, 4f, and 2d lattice sites align parallel to the c axis (12↑), while those on the 4e, 4f_{IV}, and 4f_{VI} sites align antiparallel to it (6↓).[13]

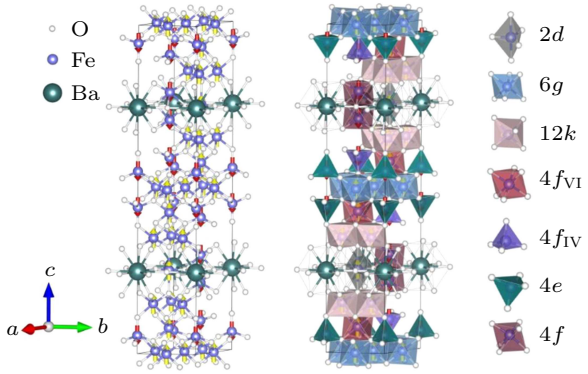


Fig. 1. Crystal structure and spin state of W-type barium hexaferrite.

Ion substitution is considered an effective method for regulating the magnetic properties of materials and expanding their applications.[14,15] Compared with the M-type ferrites, the crystal sites for cations are more abundant in W-type ferrites, increasing the flexibility of ions occupying appropriate

†Corresponding author. E-mail: wanglichen@nimte.ac.cn
‡Corresponding author. E-mail: shenbaogen@nimte.ac.cn

© 2024 Chinese Physical Society and IOP Publishing Ltd

crystal positions. To meet the requirements of various applications, many researchers have attempted to use divalent metal cations to enhance the performance of W-type hexaferrite. Yang *et al.*[16] prepared Co–Zn co-doped BaW ferrite using the sol–gel method and investigated the microwave absorption, and a maximum loss of −18 dB at 5.5 GHz was reported. $SrZn_xFe_{2-x}Fe_{16}O_{27}$ ($0 \leq x \leq 1.5$) were synthesized by the solid-phase method under low oxygen pressure by You *et al.*,[17] and the results showed that the saturation magnetization was significantly improved. For the $x = 1.0$ sample that sintered at 1250 °C, the highest M_s value of 87.7 emu/g is obtained. $BaZn_xCo_{2-x}Fe_{16}O_{27}$ ($x = 0$, 0.3, 0.5, 0.7, 0.9, 1.2) was successfully synthesized by chemical co-precipitation by Sun *et al.*,[18] and the complex permittivity and permeability of the samples were calculated for the determination of the samples in the frequency range of 1 GHz–18 GHz based on the measured data of the microwave vector network analyzer. Ali *et al.*[19] synthesized $Ba_{0.5}Sr_{0.5}Co_{2-x}Me_xFe_{16}O_{27}$ ($x = 0$, 0.5, Me = Mn, Mg, Zn, Ni) by sol–gel auto-combustion method, and the high saturated magnetization and low coercivity make them promising candidates for microwave absorbing materials. Attia *et al.*[20] reported the conduction mechanism of $BaZn_{2-x}Mg_xFe_{16}O_{27}$ ($x = 0.0$, 0.4, 0.8, 1.2, and 1.6) prepared by the conventional ceramic method. It is found that these ferrites are n-type semiconductors and their conduction process is mainly a multiple hopping conduction mechanism.

However, current research on the substitution of Fe ions is relatively scattered and not systematic enough, and the preparation of samples containing Fe^{2+} ions must be carried out under low oxygen pressure or complex heat treatment, which limits its widespread application. Therefore, in this study, the solid-phase reaction method was used to prepare divalent ion-substituted $BaMe_2Fe_{16}O_2$ (Me = Fe, Mn, Zn, Ni, Co) W-type hexagonal ferrite. The effects of different divalent cation substitutions on the magnetic and dielectric properties were analyzed using x-ray diffractometer (XRD), scanning electron microscopy (SEM), Raman, VSM, and LCR meter.

2. Experiment

2.1. Preparation of W-type ferrite

$BaMe_2Fe_{16}O_{27}$ (Me = Fe, Mn, Zn, Ni, Co) polycrystalline samples were synthesized using the solid-phase reaction method. The starting materials are $BaCO_3$ (Aladdin 99.0% purity), Fe_2O_3 (Macklin 99.0% purity), ZnO (Alfa Aesar 99.999% purity), MnO (Macklin 99.0% purity), NiO (Macklin 99.0% purity), and Co_3O_4 (Macklin 99.0% purity). The starting materials were accurately weighted according to stoichiometric ratios, and well mixed in a planetary ball mill (Nanjing Boyuntong Instrument, XGB2) with deionized water at 200 rpm for 2 hours. All the samples were sintered in a regular muffle furnace at 1300 °C for 3 hours, except for the $BaFe_{18}O_{27}$ sample was sintered in a tube furnace under the protection of a nitrogen atmosphere that can maintain the valence state of Fe^{2+} ions.[21]

2.2. Characterization

The x-ray diffractometer (XRD, Bruker D2 Phaser) equipped with Cu $K\alpha$ radiation was employed to analyze the phase structure of the synthesized samples, with step size of 0.02° and angular range of 20°–80° (30 kV, 10 mA, λ = 1.54184 Å). The microstructure analysis of the powder was performed using scanning electron microscopy (SEM, Tescan Vega Compact). Raman scattering spectra of all samples were recorded at room temperature using a confocal micro-Raman spectrometer, with laser wavelength of 532 nm and the wavenumber range of 50 cm^{-1}–900 cm^{-1} (Renishaw inVia Reflex Raman Microscope). The magnetization of the sample was measured at 300 K with the scanning magnetic field range of ±30 kOe (1 Oe = 79.5775 $A{\cdot}m^{-1}$), by using the vibration sample magnetometer option of physical properties measurement system (Quantum Design, DynaCool Cryogen-free System). The saturation magnetization (M_s) and the magnetic anisotropy field (H_a) were calculated according to the law of approach to saturation. The dielectric properties of the samples were characterized with the Agilent 4980 LCR meter.

3. Results and discussion

3.1. X-ray diffraction

Figure 2 depicts the XRD patterns of all $BaMe_2Fe_{16}O_{27}$ (Me = Fe, Mn, Zn, Ni, Co) powder samples collected at room temperature, in which the red lines are the standard BaW ferrite PDF card (PDF#75-0406). The excellent agreement between the observed peaks and the standard patterns indicates that all the samples prepared by the high-temperature solid-state method have single-phase W-type structures. The relative variation of (00l) peak intensity observed in $BaFe_{18}O_{27}$ sample can attributed to the big size plate-shaped crystalline grain as shown in Fig. 3(a), that can introduce the texture.

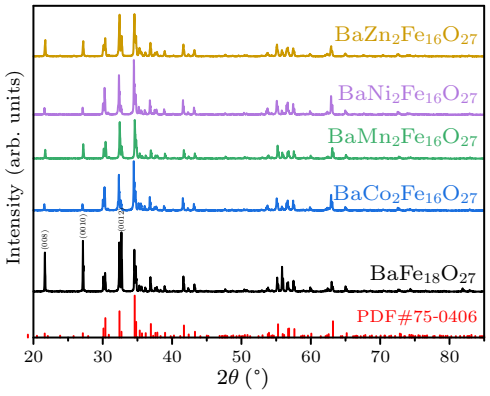


Fig. 2. XRD patterns of $BaMe_2Fe_{16}O_{27}$ (Me = Fe, Mn, Zn, Ni, Co) powders.

3.2. SEM study

The magnetic and dielectric properties of W-type hexaferrite are closely related to the microstructure. Figure 3 shows the micrograph of the obtained BaMe_2Fe$_{16}$O$_{27}$ (Me = Fe, Mn, Zn, Ni, Co) powder sample by using scanning electron microscopy (SEM). All samples have hexagonal plate-shaped grains, consistent with XRD predictions. The images show that the substitution of Fe ions by Me ions leads to significant changes in the grain microstructure, especially for the crystal grain size and the ratio of radius to axis. All samples show large average grain size, that may be due to high sinter temperature and long sinter time. The specific plate-shape structure and larger grain size are favorable for higher frequency application.[4]

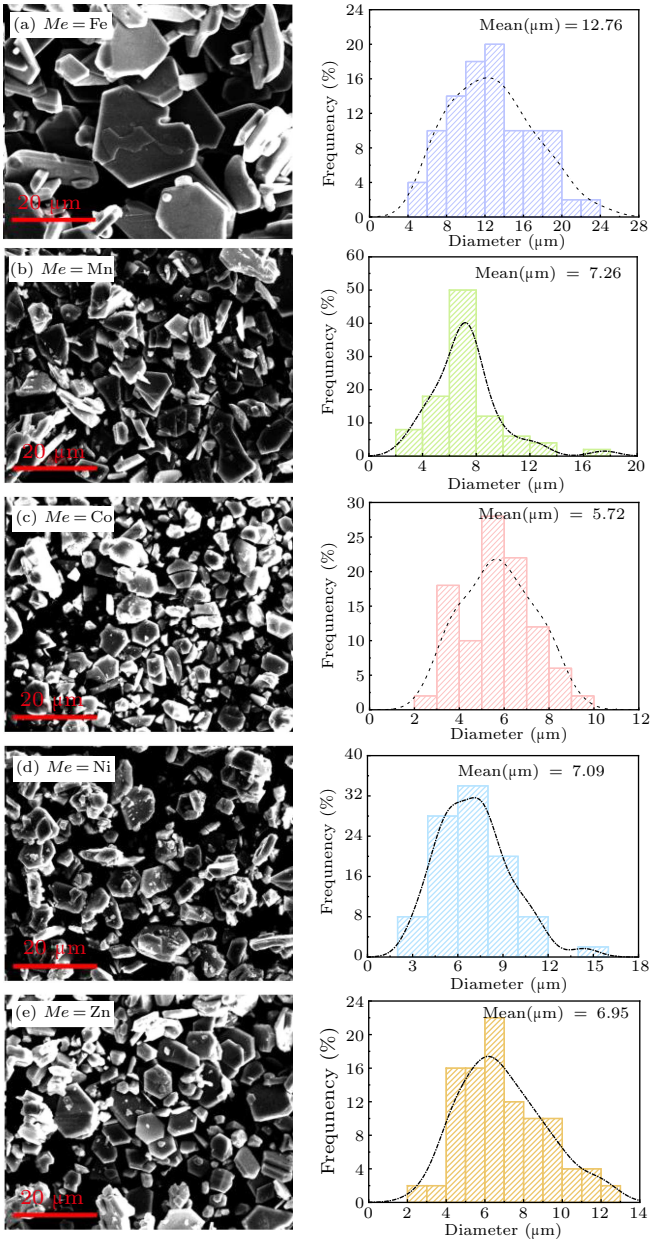


Fig. 3. SEM micrographs and grain size distribution of BaMe_2Fe$_{16}$O$_{27}$ (Me = Fe, Mn, Zn, Ni, Co) powder samples.

3.3. Raman spectra

The crystal structure was further characterized using Raman spectroscopy, which can provide information on the symmetric vibration modes of the crystal and is highly sensitive to the vibrations of atomic bonds. The W-type ferrite exhibits a hexagonal crystal structure with the space group of $D6h$ ($P63/mmc$). Group theory principles indicate 42 Raman active modes in hexagonal ferrites named as $11A_{1g}+14E_{1g}+17E_{2g}$.[22–24] Here, A and E represent symbols for one-dimensional and two-dimensional vibration modes, while g denotes symmetry concerning the center of symmetry.

The room temperature Raman spectra of BaMe_2Fe$_{16}$O$_{27}$ (Me = Fe, Mn, Zn, Ni, Co) samples are shown in Fig. 4, which were recorded in the range of 50 cm^{-1} to 900 cm^{-1}. It is evident that the shape and position of the Raman peaks are affected by the variation of the substituent ion Me^{2+}. In our experiment, Raman spectra analysis revealed ten active modes and these modes with their respective symmetries and associated sites are listed in Table 1. The peaks shown in the figure are all feature Raman peaks of W-type hexagonal ferrite, which are contributed by the vibration of metal–oxygen bonds at different interstitial positions (tetrahedral, octahedral, bipyramidal).[25]

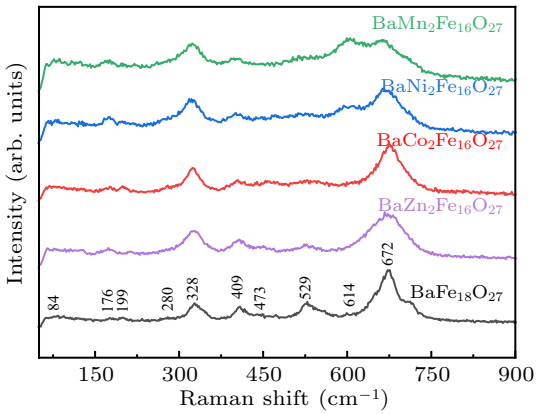


Fig. 4. Raman spectra of BaMe_2Fe$_{16}$O$_{27}$ (Me = Fe, Mn, Zn, Ni, Co).

Table 1. Raman peaks of BaMe_2Fe$_{16}$O$_{27}$ (Me = Fe, Mn, Zn, Ni, Co) in powder form.

Fe	Mn	Co	Ni	Zn	Symmetry	Assigned polyhedra
84	86	84	85	86	–	–
176	176	176	176	174	E_{1g}	spinel block
199	199	199	199	208	A_{1g}	octahedral
280	282	280	280	281	E_{2g}	octahedral (2a)
328	324	324	325	328	E_{1g}	octahedral (12k)
409	407	405	402	407	A_{1g}	octahedral (12k) dominated
473	472	458	465	451	A_{1g}	octahedral ($2a+12k$)
529	514	527	525	527	E_{1g}	octahedral (12k)
614	605	613	612	612	A_{1g}	octahedral ($4f_{VI}$)
672	665	676	665	667	A_{1g}	bipyramidal (2b)

The main peak at 665 cm^{-1}–672 cm^{-1} of the Raman spectra, is caused by the vibrations of the bipyramidal

(FeO5, 2*b* site) with A_{1g} symmetry. The vibration modes at 280 cm^{-1}–281 cm^{-1}, 451 cm^{-1}–473 cm^{-1}, 514 cm^{-1}–529 cm^{-1}, and 605 cm^{-1}–614 cm^{-1} are associated with octahedral (2*a*, $2a+12k$, 12*k*, and $4f_{VI}$ sites), respectively, and all exhibit A_{1g} symmetry. The active mode at 174 cm^{-1}–176 cm^{-1} is due to the entire spinel block vibrations, which have E_{1g} symmetry. The vibrational modes at 324 cm^{-1}–328 cm^{-1} and 402 cm^{-1}–409 cm^{-1} can be associated with the octahedra (12*k* site) and are attributed to E_{2g} and E_{1g} symmetry. In the Me^{2+} substituted samples, considerable shifts in the Raman characteristic peaks can be found. The substituted ions Mn^{2+} (0.80 Å), Zn^{2+} (0.74 Å), Ni^{2+} (0.72 Å), and Co^{2+} (0.74 Å) have different ionic radius compares with the host ions Fe^{3+} (0.64 Å) and Fe^{2+} (0.76 Å). It can be observed that the peak positions at 672 cm^{-1} (bipyramidal, FeO5, 2*b* site) shifted slightly to lower wavelength due to the substitution of Mn^{2+}, Zn^{2+}, and Ni^{2+}. The modes are all reduced in intensity and accompanied by peak broadening. This may be due to the change in ion mass and force constants (based on ion valence states, bond lengths, lattice parameters, *etc*.) due to substitution.[26] The Raman peak at 614 cm^{-1} shows a more significant shift and amplitude change in the samples substituted with Me^{2+}, the Mn^{2+} and Ni^{2+} substituted samples result in a sharper band. The Raman peak widths are highly sensitive to the substitution of magnetic structures. The maximum change in both substitutions occurs at the octahedral $4f_{IV}$ site, which may be the factor responsible for these band changes. As the substitution occurs, the peak intensity at 529 cm^{-1} decreases while the width increases. This is likely due to the local octahedral FeO_6 aberration caused by the occupation of the 12*k* site by the ion with larger radius. These results indicate that the Me^{2+} ions have successfully entered the BaW sublattice, which may affect the magnetic and dielectric properties.

3.4. Magnetic properties

The magnetic hysteresis loops measured for all $BaMe_2Fe_{16}O_{27}$ (Me = Fe, Mn, Zn, Ni, Co) samples at room temperature are depicted in Fig. 5(a). It can be seen that the hysteresis loops exhibit essentially symmetrical "S" shapes. Table 2 summarizes various magnetic parameters extracted from these loops, including saturation magnetization (M_s), coercivity (H_c), and magnetocrystalline anisotropy field (H_a). Values of M_s and H_a are obtained by the *M*–*H* curve using the law of approaching saturation.[27] The general expression of this law is

$$M = M_s\left(1-\frac{A}{H}-\frac{B}{H^2}\right)+\chi H, \tag{1}$$

where M_s represents saturation magnetization, A is the magnetic hardness coefficient, B is the magnetocrystalline anisotropy constant, H denotes the applied magnetic field, and χ is the high-field magnetization susceptibility. In the high field region, the M–$1/H^2$ relationship exhibits linearity, with parameters A and χ becoming very small and negligible. Consequently, the above equation can be simplified to

$$M = M_s\left(1-\frac{B}{H^2}\right). \tag{2}$$

For the hexagonal crystal structure with uniaxial anisotropy, B can be expressed as

$$B = \frac{H_a^2}{15} = \frac{4K_1^2}{15M_s^2}. \tag{3}$$

M_s and B are calculated from a linear fit to the law of approaching saturation, as shown in Figs. 5(b)–5(f). The magnetocrystalline anisotropy field (H_a) can be derived from Eq. (3). Compared with $BaFe_{18}O_{27}$, the magnetic measurements reveal that the M_s and H_a decrease with other Me^{2+} ion doping. This variation in M_s results from the choice of substituent ions in the insertion structure and the occupation of specific cationic sites by Me^{2+}. In W-type hexagonal ferrites, 32 Fe^{3+} ions and 4 Me^{2+} ions occupy seven different magnetic sublattices in the unit cell. The distribution and valence states of ions in the lattice contribute differently to the total magnetization intensity, which is determined by the difference between the magnetization intensity at octahedral sites and that at tetrahedral sites. Both Co^{2+} and Ni^{2+} ions show a preference for octahedral sites (2*a* and 12*k* sites) with spin directions aligned with the overall magnetic moment,[28,29] corresponding to a change in the Raman peak of 521 cm^{-1} (12*k* sites). Furthermore, their preference energy for these sites surpasses that of Fe^{3+} ions. However, since the magnetic moments of the dopant ions Ni^{2+}, Co^{2+}, and Mn^{2+} (3.0 μ_B, 4.0 μ_B, and 2.7 μ_B, respectively) are smaller than Fe^{3+} ions (5 μ_B), the substitution of spin-up Fe^{3+} ions leads to a decrease in the net magnetization, resulting in a lower saturation magnetization of the sample. The dope of Mn^{2+} to the W-type hexaferrite weakens the Fe–O–Fe super-exchange interactions, resulting in a decrease in the magnetic properties.[30] Zn^{2+} is a non-magnetic ion that tends to occupy tetrahedral sites (4*e* and $4f_{IV}$) with spin down.[13,31] Its substitution leads to a weakening of the alignment between the magnetic ions and tilting of the antiparallel alignment of the spins, which results in a reduction of the net magnetic moment. This difference may be due to variations in the evaluation method for the M_s value. The observed low coercivity can be attributed to the overgrowth of crystals at high sintering temperature, which induces a multi-domain character, leading to the disappearance of H_c.[32] Except for the Co_2W sample, the variation of the coercivity is in general

agreement with the results of the grain size variation derived from the SEM images. In addition, the coercivity is also affected by the anisotropic field. Co_2W has planar anisotropy and doping with Co^{2+} can change the anisotropy of Me_2W from c axis to c planar,[33] significantly reducing coercivity. Table 3 lists the properties of similar materials prepared by other researchers, and it can be seen that we have successfully synthesized $BaMe_2Fe_{16}O_{27}$ using a simpler solid-phase reaction method, along with an improvement in coercivity.

Table 2. Room temperature magnetic parameters of $BaMe_2Fe_{16}O_{27}$ (Me = Fe, Mn, Zn, Ni, Co) with different divalent ion substitutions.

Me	M_s (emu/g)	H_{cj} (Oe)	H_a (Oe)
Fe	95.34	375	13739.57
Co	74.90	71	10750.90
Ni	69.49	457	10700.60
Zn	72.90	439	12206.23
Mn	47.77	429	11301.48

Table 3. Findings of different researchers.

Sample	H_{cj} (Oe)	Preparation method	References
$BaZn_2Fe_{16}O_{27}$	365.85	chemical co-precipitation	[34]
$BaZn_2Fe_{16}O_{27}$	62	co-precipitation route	[35]
$BaCo_2Fe_{16}O_{27}$	130	solid-state method	[36]
$BaNi_2Fe_{16}O_{27}$	186	conventional ceramic method	[37]
$Ba_{0.5}Sr_{0.5}Co_{1.5}Mn_{0.5}Fe_{16}O_{27}$	72.53	sol–gel autocombustion	[38]

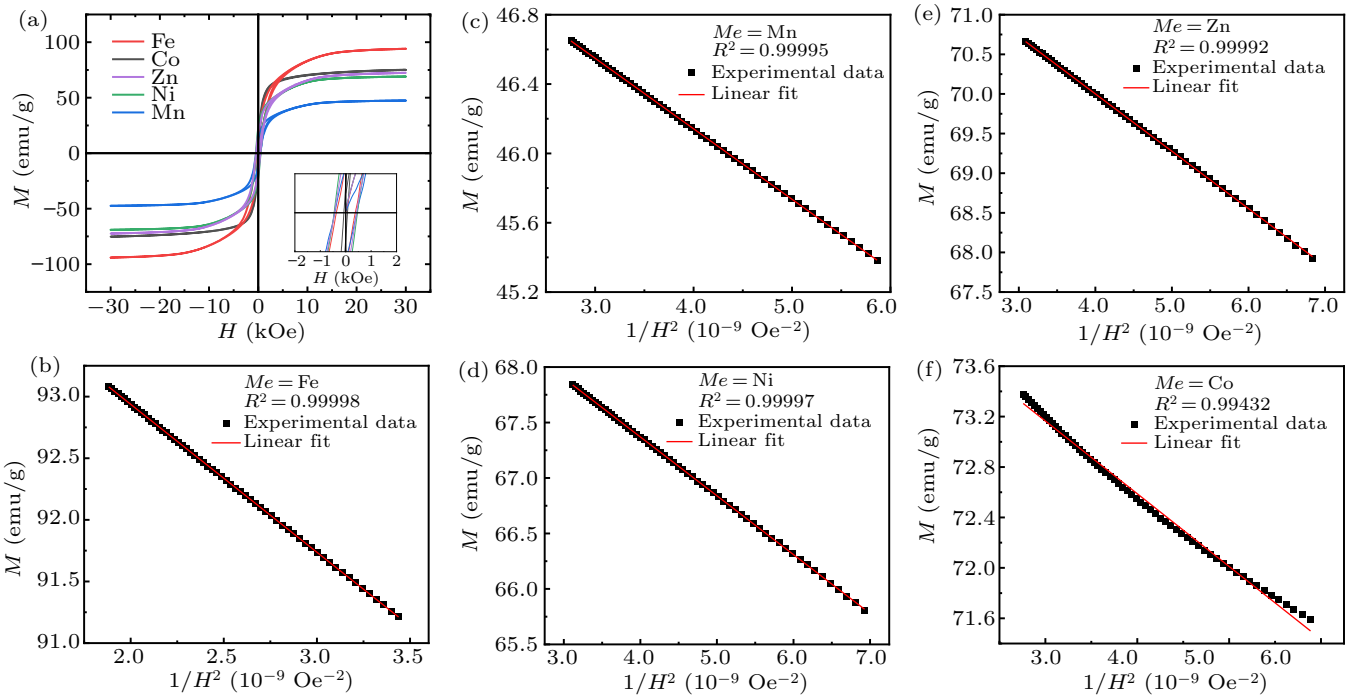


Fig. 5. (a) The M–H loops for all substituted $BaMe_2Fe_{16}O_{27}$ hexaferrite samples. (b)–(f) Fitted curves of M_s for $BaMe_2Fe_{16}O_{27}$ hexaferrite samples calculated from the law of approaching saturation.

3.5. Dielectric measurements

Figure 6 draws the frequency dependence of the dielectric constant and dielectric loss for the prepared ferrite compounds at room temperature. For all the samples, the dielectric constant and dielectric loss decrease accompanying the frequency range from 100 Hz to 1 MHz. Above 1 MHz, the dielectric permittivity almost remains unchanged. For this phenomenon, it can be attributed to that at low frequencies all the dipole relaxation can well follow the frequency of ac electric field. Therefore, a higher dielectric constant can result. At higher frequencies, however, the electron hopping between Fe^{3+} and Fe^{2+} ions lags, and part of the dipoles cannot follow the reversal of field, the samples only present a lower dielectric permittivity finally.[39] By comparing the different compositions of ferrite, it is also found that the Fe_2W-ferrite possesses the highest dielectric permittivity, which is similar to Rehman's report[40] based on Koop's theory. This could be ascribed to the fact that the Fe cations usually have mixed valence states. It increases the probability of hopping conduction and results in a high value of the dielectric constant. Higher dielectric constants lead to an enhanced skinning effect, which reduces the depth of electromagnetic wave penetration. Therefore, by replacing Fe with other divalent ions, the hopping conduction can be well suppressed. Correspondingly, the dielectric permittivity reduces dramatically, helping their application at

high frequencies. Dielectric loss is an important part of the total loss in ferrite cores.[41] Therefore, low dielectric loss is necessary for low core losses. Figure 6(b) shows the dielectric loss as a function of frequency for different compositions. The dielectric loss curve is similar to the real part of the dielectric constant as a function of frequency, which implies that the dielectric properties of ferrite can be adjusted by changing the divalent ions.

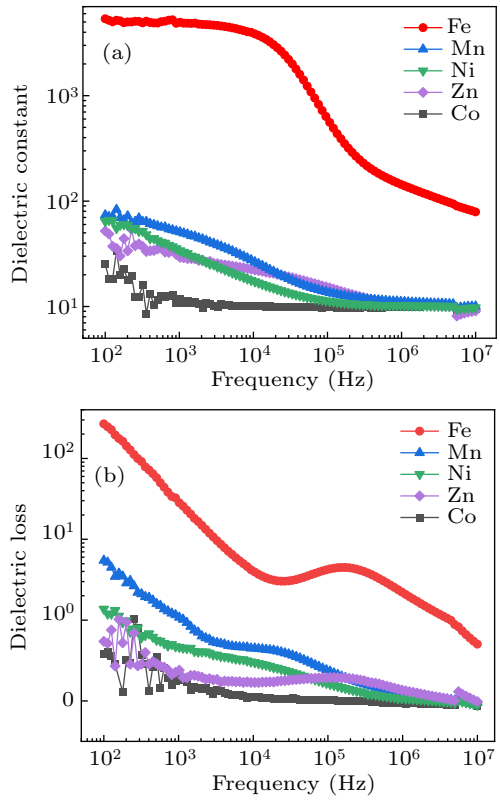


Fig. 6. (a) Variation of the real part of the dielectric constant (ε') with frequency for BaMe_2Fe$_{16}$O$_{27}$ (Me = Fe, Mn, Zn, Ni, Co) BaW ferrites. (b) Variation of dielectric loss *versus* frequency of BaMe_2Fe$_{16}$O$_{27}$ (Me = Fe, Mn, Zn, Ni, Co) BaW ferrites.

4. Conclusions

High purity W-type hexagonal ferrite BaMe_2Fe$_{16}$O$_{27}$ (Me = Fe, Mn, Zn, Ni, Co) samples with divalent ion substitution were prepared by high-temperature solid-state method, and the structure, magnetic and dielectric properties were systematically investigated. The materials exhibited hexagonal symmetry and belonged to the $P63/mmc$ space group. Raman analysis demonstrated the existence of ten active vibration modes in the wavenumber range of 50 cm^{-1}–900 cm^{-1}. The variations in peak intensity and width of Raman spectra were attributed to changes in ion substitution due to their occupancy. The variations in magnetic properties can be attributed to the magnetic moment and occupancy tendency of the substitute ion itself, and the size of the crystal grain. The dielectric constant and dielectric loss decrease as the frequency increases in the low-frequency region and it becomes a constant in the high-frequency region. Frequency hopping conduction can be well suppressed to achieve dielectric property adjustment by replacing Fe^{2+} with divalent ions. The magnetic and dielectric properties of BaMe_2Fe$_{16}$O$_{27}$ are diverse and easily tunable. Therefore, BaW hexaferrite synthesized by substituting *Me* ions is more conducive to achieve a wider frequency range of applications.

Acknowledgements

Project supported by the National Natural Science Foundation of China (Grant No. 52088101), the Kunpeng Plan of Zhejiang Province, and Ningbo Top Talent Program.

References

[1] Rathenau G, Smit J and Stuyts A 1952 *Philips Technical Review* **13** 194
[2] Pullar R C 2012 *Prog. Mater. Sci.* **57** 1191
[3] Ahmad M, Grössinger R, Kriegisch M, Kubel F and Rana M 2012 *Curr. Appl. Phys.* **12** 1413
[4] Akhtar M N, Javed S, Ahmad M, Sulong A and Khan M A 2020 *Ceramics International* **46** 7842
[5] Carvalheiras J, Novais R M, Mohseni F, Amaral J S, Seabra M P, Labrincha J A and Pullar R C 2020 *Ceramics International* **46** 5757
[6] Moon K S and Kang Y M 2017 *Ceramics International* **43** 14309
[7] Turchenko V, Bondyakov A, Trukhanov S, Fina I, Korovushkin V, Balasoiu M, Polosan S, Bozzo B, Lupu N and Trukhanov A 2023 *J. Alloys Compd.* **931** 167433
[8] Özgür Ü, Alivov Y and Morkoç H 2009 *J. Mater. Sci.: Mater. Electron.* **20** 789
[9] Iida K, Minachi Y, Masuzawa K, Kawakami M, Nishio H and Taguchi H 1999 *J. Magn. Soc. Jpn.* **23** 1093
[10] Mørch M I, Ahlburg J V, Saura-Múzquiz M, Eikeland A Z and Christensen M 2019 *IUCrJ* **6** 492
[11] Zhang J 2019 *J. Mater. Sci.: Mater. Electron.* **30** 8437
[12] Rehman A u, Shaukat S F, Akhtar M N and Ahmad M 2019 *Ceramics International* **45** 24202
[13] Albanese G, Carbucicchio M and Asti G 1976 *Appl. Phys.* **11** 81
[14] Mohammed J, Suleiman A B, Tchouank Tekou Carol T, Hafeez H Y, Sharma J, Maji P K, Kumar S G and Srivastava A K 2018 *Chin. Phys. B* **27** 128104
[15] Ali H T, Ramzan M, Arshad M I, Morley N A, Abbas M H, Yusuf M, Rehman Ur, Mahmood K, Ali A, Amin N and Ajaz-un-Nabi M 2022 *Chin. Phys. B* **31** 027502
[16] Yang X, Jin Q, Chen Z, Li Q and Liu B 2014 *J. Magn. Magn. Mater.* **367** 64
[17] You J H and Yoo S I 2018 *J. Alloys Compd.* **763** 459
[18] Sun M, Zheng J, Liang L, Sun K, Song Y and Zhao S 2015 *J. Mater. Sci.: Mater. Electron.* **26** 9970
[19] Ahmad M, Ali I, Grössinger R, Kriegisch M, Kubel F and Rana M 2013 *J. Alloys Compd.* **579** 57
[20] Attia S, El Ata A A and El Kony D 2004 *J. Magn. Magn. Mater.* **270** 142
[21] Tang J, Li D, Li Y, Liu C and Zeng J 2021 *J. Electron. Mater.* **51** 141
[22] Tahir W, Khan M A, Rasool R T, Dabagh S, Gulbadan S, Majeed A, Albalawi H, Bouzgarrou S and Mahmood K 2023 *Physica B* **659** 414872
[23] Tahir W, Khan M A, Gulbadan S, Majeed A and Mahmood K 2021 *Journal of Taibah University for Science* **15** 1196
[24] Iqbal A, Khan M A, Rasool R T, Gulbadan S, Algaradah M M, Ashraf G A, Alshahrani T, Abd-Rabboh H S M, Akhtar M N and Irfan M 2024 *Ceramics International* **50** 4446
[25] Tahir W, Khan M A, Rasool R T, Gulbadan S, Majeed A and Nasar G 2023 *J. Mater. Sci.: Mater. Electron.* **34** 1812
[26] Yar I M, Irfan M, Naheed F, Akhtar M N, Rasool R T, Ashraf G A, Gulbadan S and Khan M A 2024 *Appl. Phys. A* **130** 87
[27] Groessinger R 1981 *Phys. Status Solidi (a)* **66** 665
[28] Collomb A, Lambert-Andron B, Boucherle J and Samaras D 1986 *Phys. Status Solidi (a)* **96** 385
[29] Collomb A, Wolfers P and Obradors X 1986 *J. Magn. Magn. Mater.* **62** 57

[30] Akhtar M N, Javed S, Ahmad M, Sulong A B and Khan M A 2020 *Ceramics International* **46** 7842
[31] Collomb A and Valletregi M 1987 *Materials Research Bulletin* **22** 753
[32] Knudsen C G, Mørch M I and Christensen M 2023 *Dalton Transactions* **52** 281
[33] Su Z J, Chen Y J, Hu B L, Sokolov A S, Bennett S, Burns L, Xing X and Harris V G 2013 *J. Appl. Phys.* **113** 17B305
[34] Cao X, Guo X and Meng J 2018 *Journal of Sol–Gel Science and Technology* **85** 149
[35] Polley K, Dey S K, Kumar A and Bera J 2024 *J. Mater. Sci.: Mater. Electron.* **35** 269
[36] Li J and Sun X 2023 *Materials* **16** 5897
[37] Iqbal M A, Tahir W, Murtaza Rai G, Noor N A, Ali S and Kubra K T 2012 *Ceramics International* **38** 3757
[38] Ali A, Grössinger R, Imran M, Khan M A, Elahi A, Akhtar M N, Mustafa G, Khan M A, Ullah H, Murtaza G and Ahmad M 2017 *J. Electron. Mater.* **46** 903
[39] Kharabe R G, Devan R S, Kanamadi C M and Chougule B K 2006 *Smart Materials and Structures* **15** N36
[40] Rehman A u, Shaukat S F, Haidyrah A S, Akhtar M N and Ahmad M 2021 *Journal of Electroceramics* **46** 93
[41] Zhu J, Tseng K J and Foo C F 2000 *IEEE Trans. Magn.* **36** 3408